remote sensing

MDPI

Article

A Suitable Retrieval Algorithm of Arctic Snow Depths with AMSR-2 and Its Application to Sea Ice Thicknesses of Cryosat-2 Data

Zhaoqing Dong [1,2], Lijian Shi [2,3,*], Mingsen Lin [2,3] and Tao Zeng [2,3]

[1] National Marine Environmental Forecasting Center, Beijing 100081, China; dongzhaoqing19@mails.ucas.ac.cn
[2] National Satellite Ocean Application Service, Beijing 100081, China; mslin@mail.nsoas.org.cn (M.L.); ztao10@mail.nsoas.org.cn (T.Z.)
[3] Key Laboratory of Space Ocean Remote Sensing and Application (MNR), Beijing 100081, China
* Correspondence: shilj@mail.nsoas.org.cn; Tel.: +86-010-8248-1859

Abstract: Arctic sea ice and snow affect the energy balance of the global climate system through the radiation budget. Accurate determination of the snow cover over Arctic sea ice is significant for the retrieval of the sea ice thickness (SIT). In this study, we developed a new snow depth retrieval method over Arctic sea ice with a long short-term memory (LSTM) deep learning algorithm based on Operation IceBridge (OIB) snow depth data and brightness temperature data of AMSR-2 passive microwave radiometers. We compared climatology products (modified W99 and AWI), altimeter products (Kwok) and microwave radiometer products (Bremen, Neural Network and LSTM). The climatology products and altimeter products are completely independent of the OIB data used for training, while microwave radiometer products are not completely independent of the OIB data. We also compared the SITs retrieved from the above different snow depth products based on Cryosat-2 radar altimeter data. First, the snow depth spatial patterns for all products are in broad agreement, but the temporal evolution patterns are distinct. Snow products of microwave radiometers, such as Bremen, Neural Network and LSTM snow depth products, show thicker snow in early winter with respect to the climatology snow depth products and the altimeter snow depth product, especially in the multiyear ice (MYI) region. In addition, the differences in all snow depth products are relatively large in the early winter and relatively small in spring. Compared with the OIB and IceBird observation data (April 2019), the snow depth retrieved by the LSTM algorithm is better than that retrieved by the other algorithms in terms of accuracy, with a correlation of 0.55 (0.90), a root mean square error (RMSE) of 0.06 m (0.05 m) and a mean absolute error (MAE) of 0.05 m (0.04 m). The spatial pattern and seasonal variation of the SITs retrieved from different snow depths are basically consistent. The total sea ice decreases first and then thickens as the seasons change. Compared with the OIB SIT in April 2019, the SIT retrieved by the LSTM snow depth is superior to that retrieved by the other SIT products in terms of accuracy, with the highest correlation of 0.46, the lowest RMSE of 0.59 m and the lowest MAE of 0.44 m. In general, it is promising to retrieve Arctic snow depth using the LSTM algorithm, but the retrieval of snow depth over MYI still needs to be verified with more measured data, especially in early winter.

Keywords: snow depth; sea ice thickness; AMSR-2; CryoSat-2; Arctic; LSTM

Citation: Dong, Z.; Shi, L.; Lin, M.; Zeng, T. A Suitable Retrieval Algorithm of Arctic Snow Depths with AMSR-2 and Its Application to Sea Ice Thicknesses of Cryosat-2 Data. *Remote Sens.* **2022**, *14*, 1041. https://doi.org/10.3390/rs14041041

Academic Editor: Yi Luo

Received: 19 December 2021
Accepted: 16 February 2022
Published: 21 February 2022

1. Introduction

The extent and thickness of Arctic sea ice are dramatically decreasing due to global warming [1–4]. Arctic sea ice and snow are important factors of the global climate system, playing key roles in maintaining the energy balance of the global climate system, so they have attracted increasing attention and research. Sea ice regulates the overall radiation budget of the polar region through ice-albedo feedback [5,6], and snow has a higher reflectivity and much lower thermal conductivity than sea ice [7,8]. As snow accumulates,

it increases surface albedo, leading to reduced solar radiation absorbed by sea ice (except during the polar night) [9]. Even a few centimeters of snow will reduce the heat exchange between the ocean and atmosphere through sea ice. Snow slows the growth of sea ice in winter and the melting of sea ice in summer [10,11]. As Arctic snow melts, it may form melt ponds, enhancing the solar radiation absorbed by sea ice and the melting of the ice pack [12,13]. Therefore, the changes in sea ice and snow are intricately linked. Accurate knowledge of sea ice thickness (SIT) and snow depth is essential for understanding regional and global climate change.

SIT is one of the most important parameters of sea ice and the third dimension to research for sea ice change. An accurate acquisition of SIT is of great significance in studying sea ice change. Satellite altimeters have proven to provide information about the sea ice thickness distribution in the Arctic [14] and the Antarctic [15]. To retrieve SIT from freeboard measurements by radar altimeters, snow depth has to be known with high accuracy. The uncertainty in snow depth contributes significantly to the uncertainty in SIT [16,17]. To calculate the SIT from sea ice freeboards, the Warren climatology product (hereafter referred to as W99) is often used [18–22]. It relies on the direct measurement of snow depth by many Soviet drifting buoys deployed over multiyear ice (MYI) from 1954 to 1991 [23]. Due to the lower snow depth on first-year ice (FYI), the W99 snow depth over FYI is multiplied by a correction coefficient of 0.5 or 0.7 to correct the snow depth over FYI [24,25]. However, the Arctic has undergone rapid environmental changes in the past three decades, with an intensification of Arctic warming and a rapid decrease in sea ice extent and thickness, especially MYI. Webster et al. [26] analyzed spring snow depth measurements over the central Arctic and the Canadian Archipelago obtained from the NASA Operation IceBridge (OIB) campaign for the 2009–2013 period and compared them with W99. They found a decline in snow depth of 37% over FYI and more than 50% over MYI. Thus, this climatology cannot represent the current snow state. Moreover, these data are collected mostly over MYI with low spatial resolution and do not present any interannual variation [27]. Therefore, the accurate retrieval of snow depth in the Arctic basin can not only reduce the uncertainty in SIT retrieved by satellite altimetry but also be used to evaluate the snow depth simulated by numerical weather prediction models and climate system models to improve the prediction of sea ice and climate.

Different from observations with infrared and visible sensors, microwave sensors can be used to provide all-weather, and all-time continuous observations in polar regions and are important means of ice and snow observations in polar regions. At present, the retrieval of snow depth mainly depends on passive microwave radiometers. The existing retrieval algorithms are mainly divided into two categories: algorithms that rely on the empirical relationship between field-measured data and brightness temperature measurements by satellites, including multilinear regression algorithms [28–34] and neural network algorithms [9,35], and algorithms that rely on radiative transfer models [36–39]. Markus and Cavalieri [28] developed the first algorithm to retrieve snow depth on sea ice, which used the empirical relationship between the gradient ratio of 19.4 and 37.0 GHz in the Sensor Microwave/Imager (SSM/I) and the field-measured snow depth to retrieve the Antarctic snow depth in 1998. Comiso et al. [29] modified the algorithm coefficients of Markus and Cavalieri (1998) to match the Advanced Microwave Scanning Radiometer for EOS (AMSR-E). The retrieved AMSR-E snow depth product is distributed by the National Snow and Ice Data Center (NSIDC). The NSIDC released the snow depth operational product relying on AMSR-2 in December 2018 [30]. Because the microwave signals from MYI and thick snow are similar, the snow depth products of AMSR-E/AMSR-2 provided by NSIDC are limited to the whole Antarctic region and FYI region of the Arctic with no snow depth data on MYI. Markus et al. [31] found that the lower frequencies of AMSR-E/AMSR-2 (6.9 GHz) achieve the retrieval of snow depths exceeding 50 cm, where the 36.5 GHz channel becomes saturated. Rostosky et al. [32] used the brightness temperature data of AMSR-E and AMSR-2 to analyze the correlation between the gradient ratio of different channels and NASA's OIB snow depth and selected a gradient ratio (GR (18.7/6.9)) of 18.7

and 6.9 GHz vertically polarized channels for statistical regression with OIB data. A new formula is suitable for retrieving the snow depth of FYI and MYI. The errors between the retrieval results and the OIB data on FYI and MYI are 3.7 and 5 cm, respectively. However, owing to the OIB project conducted in March and April of each year, the snow depth on MYI retrieved by the algorithm is applicable to only March and April [32]. Kilic et al. [33] determined the channel combination that can be used to retrieve snow depth by comparing the correlation between the brightness temperature of AMSR-2 and OIB snow depth and then determined that the coefficient of the multilinear regression formula relied on ice mass balance buoys (IMBs) and the brightness temperature of AMSR-2. Li et al. [34] simulated the sensitivities of the brightness temperatures from the FengYun-3B/Microwave Radiometer Imager (FY3B/MWRI) to changes in snow depth using the Microwave Emission Model of Layered Snowpacks (MEMLS). The factors most sensitive to snow depth were determined for snow depth retrieval, and the bias and standard deviation of the algorithm were 2.89 and 2.6 cm on FYI, respectively, and 1.44 and 4.53 cm on MYI, respectively.

Through many decades of effort, the application of machine learning algorithms has been increasingly expanded to include the retrieval of snow depth. Braakmann-Folgmann and Donlon [35] explored a new approach to retrieve snow depth on sea ice from brightness temperature by AMSR-2 using a neural network approach. They evaluated the results from snow depth measurements of the OIB snow radar and compared them to three conventional microwave radiometer algorithms. They found that the algorithm is suitable for retrieving snow depth on FYI and MYI. Different from the retrieval error for OIB snow depths, the retrieval error is approximately 1 cm [35]. Liu et al. [9] established a deep neural network model for retrieving snow depth on FYI and MYI on the basis of IMB ice buoy data and SSMI/S microwave radiometer brightness temperature data. The average deviation and root mean square error (RMSE) between the retrieved snow depth and IMB data are 0.1 and 9.8 cm, respectively.

Satellite altimeters show good potential for retrieving snow depth. Guerreiro et al. [40] found that the combination of radar altimeters operating at Ka and Ku-band frequencies is suitable for retrieving snow depth over Arctic sea ice. The results show good agreement with OIB snow depth measurements. The retrieval area is limited to observations below 81.5°N, excluding the central Arctic. Kwok et al. [41] retrieved snow depth over Arctic sea ice using the difference between the reflection interface of the ICESat-2 laser altimeter and Cryosat-2 radar altimeter. Their results are within a few centimeters of the snow depth measured by OIB in April 2019. They also compared the SIT using the retrieved snow depth and the modified climatology. In contrast, the modified climatology snow depth and its SIT are higher by approximately 5 cm and 0.33 m, respectively, although these differences are not uniform throughout the season.

In this study, we explored a snow depth retrieval method with a long short-term memory (LSTM) deep learning algorithm over Arctic sea ice, relying on brightness temperatures acquired by AMSR-2 and snow depth measurements from the OIB snow radar. Based on snow depth measurements from OIB as validation data, we compared different snow depth products retrieved by various algorithms and satellite sources. We also compared the SIT retrieved by different snow depth products on the basis of Cryosat-2 radar altimeter data and evaluated the SIT of the OIB. In Section 2, the data used in this study are introduced. In Section 3, we introduce the LSTM neural network and the retrieval process of SIT. Then, we discuss the comparative analysis of different snow depth products and retrieved SIT in Section 4. Section 5 summarizes the conclusions of this study.

2. Data

2.1. Microwave Radiometer Data

The Advanced Microwave Scanning Radiometer 2 (AMSR-2) is a sensor on the GCOM-W1 satellite launched by The Japan Aerospace Exploration Agency (JAXA) in 2012 to provide continuous global observations of the Earth's water and energy cycles. The brightness temperatures of vertical (V) and horizontal (H) polarization were measured at seven

frequencies (6.9, 7.3, 10.7, 18.7, 23.8, 36.5 and 89.0 GHz) [42]. The AMSR-2 data are the daily averaged grid product of ascending orbit and descending orbit with the 25 km standard polar stereographic grid of the National Snow and Ice Data Center (NSIDC). The projection plane was specified by NSIDC to Earth's surface at 70 degrees northern and southern latitudes with or no distortion in the marginal ice zone [43–45]. Here the mean of the ascending and descending swaths is used. The AMSR-2 brightness temperatures are calibrated to AMSR-E brightness temperatures using the calibration coefficients proposed by Du et al. [32,42]. We carried out data matchup between AMSR-2 data and OIB data with a spatial window of 25 km and a temporal window of 1 calendar day (with respect to UTC).

2.2. Radar Altimeter Data

CryoSat-2 (CS-2) is a radar altimetry mission launched on 8 April 2010 to monitor variations in the thickness of the Earth's marine ice cover and continental ice sheets [46]. The main payload of CS-2 is a Ku-band synthetic aperture interferometric radar altimeter (SIRAL), which uses three different measurement modes with low-resolution mode (LRM), synthetic aperture radar (SAR) mode and synthetic aperture radar interferometric (SARIn) mode. The SAR mode is carried out with high-resolution measurements of floating sea ice and land ice sheets, enabling the indirect measurement of ice thickness, using a measurement footprint of 0.3 × 1.5 km in the along and across-track directions, respectively. In SAR mode, the echoes reflected from the Earth's surface are sampled in 256 range bins, and the time interval of each range bin is 1.563 ns (0.234 m). The European Space Agency (ESA) offers L1, L2 and L2I products. The L1B files contain geolocated echo waveforms, range corrections and flags of the radar altimeter SIRAL. We use SAR mode L1B data to retrieve Arctic sea ice thickness from October 2018 to April 2019.

2.3. Airborne Data

The airborne OIB experiment is an aerial remote sensing observation project over polar regions started by the National Aeronautics and Space Administration (NASA) in 2009. Its initial purpose is to compensate for the data gap existing during the operation of ICESat and ICESat-2 satellites and to carry out large-scale sea ice detection experiments in the Arctic from March to May and in the Antarctic from October to November every year. The experiment mainly relies on an airborne topographic mapper (ATM), a digital mapping system camera (DMS) and snow radar. The ATM is used to obtain the surface height with a spatial resolution of 1 m and absolute elevation accuracy of 0.1 m [47,48]. Snow radar is used to measure snow depth with a spatial resolution of 40 m and vertical resolution of 0.06 m [48,49]. In this study, because AMSR-2 was launched in 2012, we used airborne OIB snow depth data from 2013 to 2018 to develop the retrieval model of Arctic snow depth while using OIB snow depth in 2019 as test data.

Observations of snow depth on sea ice were collected by airborne frequency-modulated continuous-wave (FMCW) ultrawideband radar during the Alfred Wegener Institute's (AWI) IceBird campaigns in April 2019. The data consist of five surveys, some with overlapping segments at low and high altitudes, spanning sea-ice-covered areas in the Lincoln Sea, Central Arctic Ocean, as well as the Beaufort Sea. For each flight, the geolocated snow depth data using an algorithm based on signal peakiness are provided with a point spacing of approximately 4–5 m for low-altitude flights and 7–9 m for high-altitude flights. The IceBird snow radar has a smaller footprint than the OIB snow radar. Each snow depth value represents the average depth within the radar footprint that has a theoretical smooth surface cross/along-track diameter of 2.6/1.0 m at low altitude and 7.2/5.1 m at the high altitude [50]. We also used IceBird snow depth data (April 2019) that is completely independent of OIB for validating all snow depth products.

Figure 1 shows the flight tracks and the measured snow depths from OIB (from March 2013 to April 2019) and the IceBird campaign (April 2019). We simply overlaid the snow depths of intersecting track footprints. To be consistent with the retrieval algorithm of the CS-2 SIT, we calculated the OIB SIT in April 2019 based on hydrostatic equilib-

rium, with seawater density (1024 kg/m^3), FYI density (916.7 kg/m^3) and MYI density (882 kg/m^3) [20,51], as well as the total sea ice freeboard measured by ATM and snow depth measured by snow radar in April 2019.

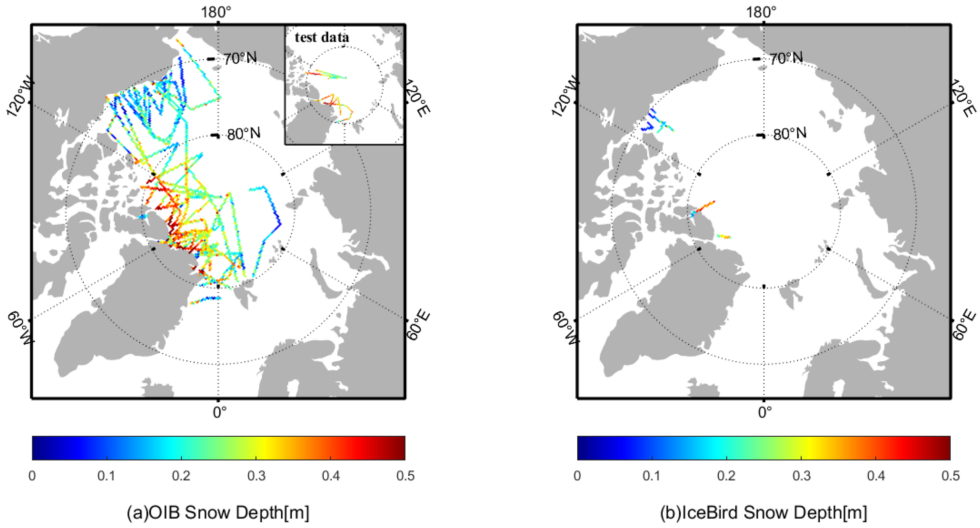

Figure 1. Airborne snow depth map: (**a**) Operation IceBridge (OIB) from March 2013 to April 2019, the sub-figure on the top right shows the OIB data used to test model and other snow depth products. (**b**) IceBird in April 2019.

2.4. Snow Depth Products

In this section, we introduce the snow depth products used in the study, including modified W99, AWI, Bremen, Kwok and Neural Network snow depth. However, the spatial and temporal resolution varies considerably between products. Details on resolution and grids are provided in Table 1.

Table 1. Summary of current snow depth products.

Product	Temporal Resolution	Spatial Grid	Projection Type	Data Type	Reference
Modified W99	monthly	6.25 km	Polar stereographic grid	Climatology	Warren et al. (1999)
AWI	monthly	25 km	EASE2-Grid	Climatology	Stefan Hendricks et al. (2020)
Bremen	daily	25 km	Polar stereographic grid	Passive satellite-based	Rostosky et al. (2018)
Kwok	monthly	25 km	Up to 88.5°N	Active satellite-based	Kwok er al. (2020)
Neural Network	daily	25 km	Polar stereographic grid	Passive satellite-based	Anne Braakmann-Folgmann et al. (2019)

2.4.1. Modified W99 Snow Depth

Based on the snow depth and density measured at Soviet drifting stations on multiyear Arctic sea ice from 1954 to 1991, a two-dimensional quadratic model named W99 Climatology Snow Depth model is fitted to represent the geographical and seasonal variation in snow depth for a particular month, irrespective of the year [23]. Because the observation data are mainly focused on MYI, the fitting results yield unrealistic snow depth over FYI. Therefore, the snow depth of W99 over FYI was modified by multiplying a coefficient of 0.5 and then we called it the modified W99 [25]. In addition, the W99 climatology is presented as a two-dimensional quadratic fit valid for the central Arctic Basin. We only researched W99 from the central Arctic; that is, the region weight factor of W99 is 1. Since the data set of ice type is time-dependent, the modified W99 contains temporal and spatial variations. Since the spatial resolution of the original W99 data is 6.25 km, we resample it to the 25 km DSIDC polar stereographic grid to be consistent with other snow depth products.

2.4.2. AWI Snow Depth

Hendricks et al. [52] merged the W99 climatology snow depth and the AMSR-2 snow depth of the University of Bremen to obtain a composite snow depth product (hereafter referred to as AWI). They created a regional weight factor that ensures a smooth transition between the inner Arctic Basin domain and the area where the AMSR-2 data are used. When the regional weight factor is 1, it means that the warren snow depth is valid; when it is 0, it means that it is invalid. It is common practice to modify the W99 snow climatology by reducing its value by 50% over FYI in the central Arctic. However, scaling should not be applied to the AMSR-2 snow depth, and only the snow depth contribution from the W99 climatology should be scaled. FYI and MYI were discriminated based on Daily Sea Ice Type Analysis from the OSI SAF EUMETSAT and Sea Ice Type (Interim) Climate Data Record. The AWI snow depth data are the monthly averaged grid product using Equal-Area Scalable Earth Grid version 2 (EASE2-Grid) for the northern hemisphere with a resolution of 25 km. We transformed it to the 25 km DSIDC polar stereographic grid using nearest interpolation.

2.4.3. Bremen Snow Depth

Rostosky et al. [32] analyzed the correlation between the gradient ratio of different channels and OIB snow depth data and tried to expand the snow depth retrieval onto MYI. The gradient ratios of 18.7 and 6.9 GHz vertically polarized channels (GR (18.7/6.9)) are applied for statistical regression with OIB data, which yields new formulas for the retrieval of snow depth on FYI and MYI (hereafter referred to as Bremen). This correction of brightness temperature is necessary since we are interested in the change in brightness temperature caused by only snow cover. Otherwise, open water is the dominant signal in the observed brightness temperature.

Since the OIB flight is conducted in March and April of every year in the Arctic, the retrieved snow depth on the MYI of the algorithm is only applicable to March and April of spring. To address the uncertainty introduced by the limited OIB sample size, they performed the regression for every possible 4-year combination between 2009 and 2015 (2009, 2010, 2011, 2014, 2015) and then calculated from the standard deviation of the regression coefficients over the five results. They used the Gaussian error propagation model to calculate the uncertainty of the contributing parameters [32,53]. The Bremen snow depth data are the daily averaged 25 km NSIDC polar stereographic grid product. We generated monthly average products by averaging daily average products.

2.4.4. Kwok Snow Depth

Kwok et al. [41] present the first examination of snow depth over Arctic sea ice estimates from differencing satellite lidar (ICESat2) and radar (CryoSat-2) freeboards. These estimates cover the period between October 2018 and April 2019 (hereafter referred to as Kwok). The Kwok snow depth data is the 25 km averaged grid product with a temporal resolution of 1 month. To compare with other snow depth products, we unified it to the 25 km DSIDC polar stereographic grid. The valid region of Kwok snow depth data is the Arctic Ocean, which is defined as the region bounded by the gateway into the Pacific Ocean (Bering Strait), Canadian Arctic Archipelago (CAA), Greenland (Flam Strait) and Barents Sea.

2.4.5. Neural Network Snow Depth

Braakmann-Folgmann et al. [35] designed an artificial neural network model to retrieve Arctic snow depth (hereafter referred to as Neural Network), relied on gradient ratios (*GR* (36.5/18.7) and *GR* (18.7/6.9)) and polarization ratios (*PR* (36.5)) of the AMSR-2 brightness temperature. They also added SMOS (The Soil Moisture and Ocean Salinity) satellite brightness temperature data to train the snow depth model and finally determine AMSR-2 and AMSR-2 + SMOS neural network models. These algorithms do not need the input of sea ice type data, which reduces the uncertainty in the retrieved snow depth over Arctic sea ice. The neural network snow depth data are the daily averaged 25 km NSIDC polar

stereographic grid product. We generated monthly average products by averaging daily average products. We compared the neural network snow depth data with modified W99, AWI, Bremen and LSTM snow depth data based on the quasi-same time resolution and the consistent spatial resolution. All results are based on the region that modified W99 and AWI have in common.

2.5. Auxiliary Data

In this study, we use auxiliary data, including the sea ice concentration (SIC), sea ice type, snow density and mean sea surface height data (MSS). The SIC and sea ice type are released by the European Organization for Meteorological Satellites (EUMETSAT) Ocean and Sea Ice SAF (OSI-SAF). We used the Global Sea Ice Concentration (SSMIS) data (version OSI-401-b) and the Global Sea Ice Type data (version OSI-403-b), which were the daily averaged grid products with the 10 km Lambert Azimuthal Grid. Sea ice type data are used to distinguish FYI and MYI. Mallet et al. [54] found that this snow density relationship served to minimize sea ice thickness differences at the start of the growth season and better enable the comparison of growth rates. The density equation of snow is shown in Equation (1) [54].

$$\rho_s = 6.50t + 274.51 \quad (1)$$

where t represents the number of months since October.

Figure 2 shows the snow density proposed by Mallet et al. The calculation of sea ice freeboard requires us to know the instantaneous elevation of the ocean surface beneath sea ice floes, which can be obtained by interpolating between lead tie points [55]. We employed DTU18 MSS data from the Technical University of Denmark to eliminate errors due to unresolved gravity features, intersatellite biases and remaining satellite orbit errors, which can precisely determine the instantaneous elevation of lead [56].

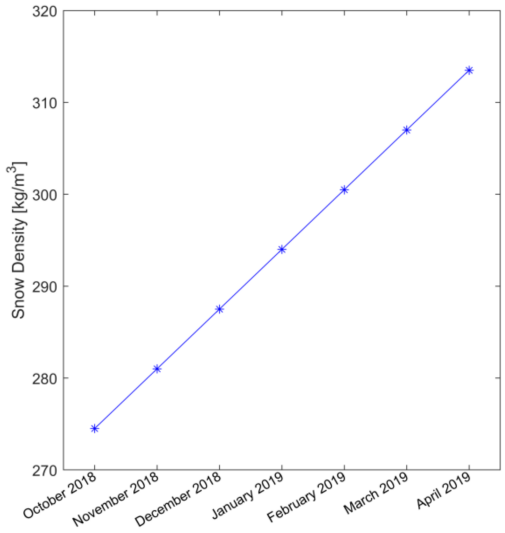

Figure 2. Time series of snow density.

3. Methods

3.1. Snow Depth Retrieval Method

Most current studies use regression methods to find the linear relationship between OIB snow depth and gradient ratio, and those methods cannot capture the nonlinear relationship between snow depth and brightness temperature. A deep learning algorithm can approximate high-dimensional functions, which is beneficial for discovering the nonlinear relationship between snow depth and brightness temperature. LSTM is a special recurrent neural network (RNN). It uses a memory module to replace the traditional implicit node, which is applicable to processing highly time-dependent problems. The formation

of a snow layer on sea ice has obvious periodicity, and the accumulation is a highly time-dependent process. Therefore, the LSTM neural network is applied to predict snow depth on sea ice. In this study, we used vertical polarization brightness temperatures of 6.9, 18.7 and 36.5 GHz and horizontal polarization brightness temperatures of 36.5 GHz. All the brightness temperatures needed to be corrected since we are interested in the change in brightness temperature due to only snow cover; otherwise, the open-water part would dominate the signal, as shown in Equation (2) [35]. We input three factors to train the retrieval model of snow depth, namely, the gradient ratios (GR (36.5/18.7) and *GR* (18.7/6.9)) and polarization ratios (PR (36.5)) of the AMSR-2 brightness temperature. Equations (3)–(5) show the calculation formulas for the gradient ratios and polarization ratios.

$$T_{b_{ice}}(f,p) = \frac{T_b(f,p) - (1 - SIC) * T_{bOW}(f,p)}{SIC} \tag{2}$$

where T_{bice} (f, p) is the corrected brightness temperature of sea ice with observation frequency f and polarization p, T_b (f, p) is the uncorrected brightness temperature of sea ice with observation frequency f and polarization p, T_{bOW} (f, p) is the open-water tie point for frequency f and polarization p using open-water tie-points derived by Ivanova et al. [57], T_{bOW} (18.7 V) = 183.72 K is the open-water tie point for frequency 18.7 GHz and vertical polarization, T_{bOW} (6.9 V) = 161.35 K is the open-water tie point for frequency 6.9 GHz and vertical polarization and SIC is the sea ice concentration.

$$GR(18.7/6.9) = \frac{T_{b_{ice}}(18.7V) - T_{b_{ice}}(6.9V)}{T_{b_{ice}}(18.7V) + T_{b_{ice}}(6.9V)} \tag{3}$$

$$GR(36.5/18.7) = \frac{T_{b_{ice}}(36.5V) - T_{b_{ice}}(18.7V)}{T_{b_{ice}}(36.5V) + T_{b_{ice}}(18.7V)} \tag{4}$$

$$PR(36.5) = \frac{T_{b_{ice}}(36.5V) - T_{b_{ice}}(36.5H)}{T_{b_{ice}}(36.5V) + T_{b_{ice}}(36.5H)} \tag{5}$$

where *GR* (18.7/6.9) is the gradient ratio of 18.7 and 6.9 GHz vertical polarization, *GR* (36.5/18.7) is the gradient ratio of 36.5 and 18.7 GHz vertical polarization, *PR* (36.5) represents a polarization ratio of 36.5 GHz vertical and horizontal polarization, T_{bice} (6.9 V), T_{bice} (18.7 V), T_{bice} (36.5 V) and T_{bice} (36.5H) are corrected with respect to the influence of water using Equation (2).

The LSTM neural unit is optimized on the basis of the RNN by adding control gates inside the units and adding new units to enable LSTM to remember and retain historical information. The whole neural unit is controlled by the input gate, the forget gate and the output gate. The internal structure of the LSTM neural unit at three consecutive times is illustrated in Figure 3. Equations (6)–(11) show the internal operations followed by neural units:

$$f_t = S(W_f \cdot [h_{t-1}, x_t] + b_f) \tag{6}$$

$$i_t = S(W_i \cdot [h_{t-1}, x_t] + b_i) \tag{7}$$

$$\widetilde{C}_t = \tanh(W_C \cdot [h_{t-1}, x_t] + b_C) \tag{8}$$

$$C_t = f_t * C_{t-1} + i_t * \widetilde{C}_t \tag{9}$$

$$O_t = S(W_O \cdot [h_{t-1}, x_t] + b_O) \tag{10}$$

$$h_t = O_t * \tanh(C_t) \tag{11}$$

where x is the 3×1 input vector of the neural unit; t = 1, is the time step length; h is the 10×1 output vector of the neural unit; C is the cell state; S and tanh are both activation functions, representing sigmoid function and hyperbolic tangent function, respectively; f, i and O are the forget gate, the input gate and the output gate, respectively; and W and b are

the weight and the deviation matrix, respectively. W_{fx}, W_{ix}, W_{Ox}, W_{Cx} are the 10 × 3 matrix. b is the 10 × 1 vector.

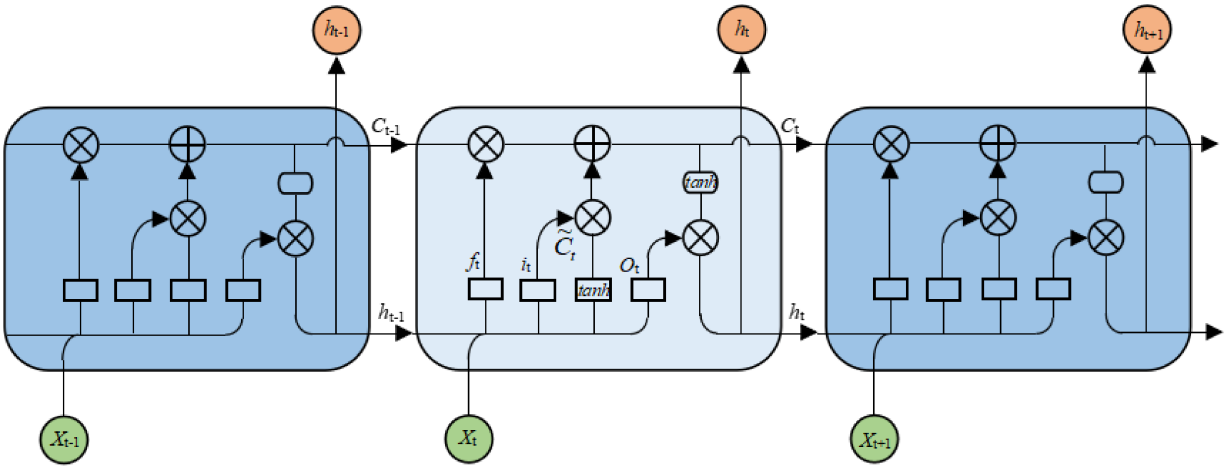

Figure 3. Structure of the LSTM neural unit.

The forget gate of the previous cell's output selects the amount of information of the previous cell to be included. The output is a number in [0, 1], which is multiplied (pointwise) by the previous cell state C_{t-1}. The input gate decides what new information is to be added to the cell. It takes two inputs, h_{t-1} and x_t. The tanh layer creates a vector $\widetilde{C}_t$ of the new candidate values. Together, these two layers determine the information to be stored in the cell state. The result is then added with the result of the forget gate multiplied by the previous cell state ($f_t * C_{t-1}$) to produce the current cell state, C_t. Next, the output of the cell is calculated using a sigmoid and tanh layer. The output gate decides which part of the cell state will be present in the output, whereas the tanh layer shifts the output in the range of $[-1, 1]$. The results of the two layers undergo pointwise multiplication to produce the output h_t of the cell.

The framework of the LSTM model is listed in Figure 4. The LSTM model consists of an input layer, an LSTM layer (10 units) and an output layer. The activation function of the LSTM layer is a sigmoid function, and the loss function is the mean absolute percentage error of the retrieval of snow depth and snow depth measurement from OIB, as shown in Equation (12). The batch size is 30, with a number of 250 epochs. The Adam algorithm is used to optimize the training process until the model converges [58]. An 80% snow depth measurement from OIB from 2013 to 2018 is used as the training data (2573 valid grid points), and the remaining 20% is the validation data (644 valid grid points). As the Kwok snow depth data is only available from October 2018 to April 2019, we keep the OIB snow depth data from April 2019 as test data (228 valid grid points). We assume that the OIB measurements are independent from year to year and thus treat the measurements from 2019 as an independent data set. The time of test data is different from the training data, which indicates the inter-comparison is independent of the OIB training. The learning curves for the LSTM model are presented in Figure 5. The model training and validation loss converged well, and no overfitting of the training data could be observed. The evaluation of the test set resulted in a final *MAPE* of approximately 31%.

$$MAPE = \sum_{t=1}^{n} \left| \frac{sd_{OIB} - sd_{predicted}}{sd_{OIB}} \right| \times \frac{100\%}{n} \quad (12)$$

where sd_{OIB} is the measured snow depth of OIB, $sd_{predicted}$ is the predicted snow depth of the LSTM and n is the number of validation data.

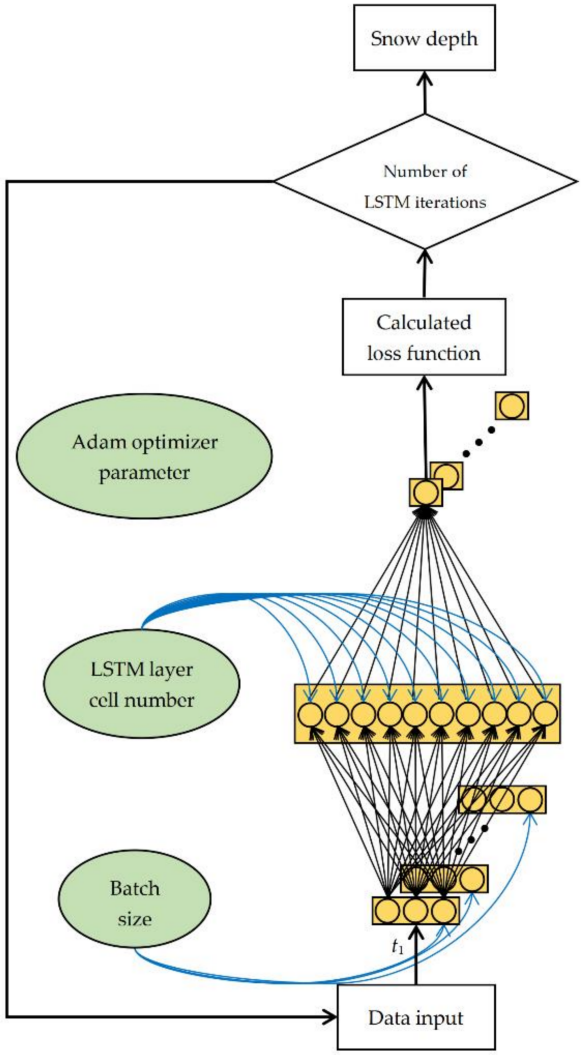

Figure 4. Framework of the LSTM model.

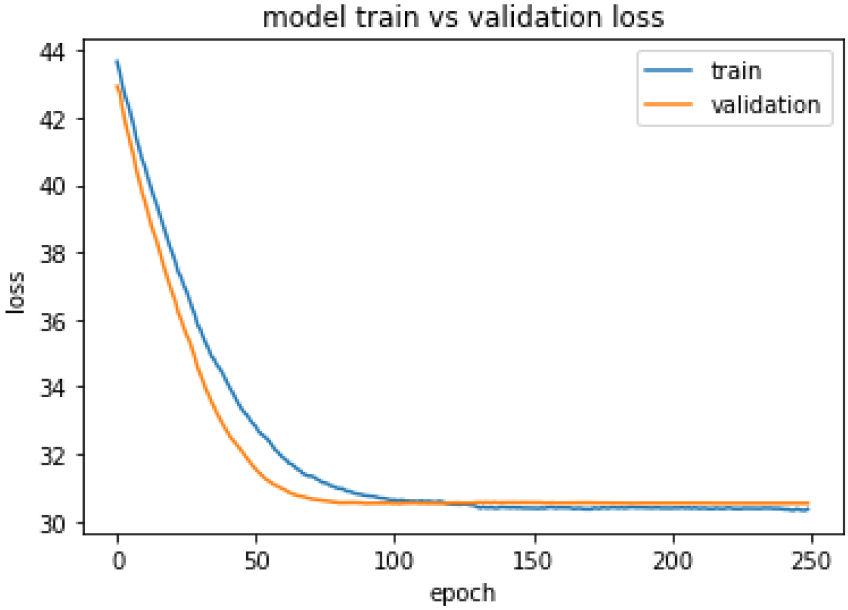

Figure 5. Evaluation of the training of the LSTM model.

3.2. Retrieval of Sea Ice Thickness

The SIT retrieval generally follows the methods described in Ricker et al. [21]. Figure 6 shows the technical process of SIT retrieval relying on CryoSat-2 L1B. The flow for the retrieval of SIT is as follows. The snow depth products are used as the input data in Steps 5 and 6.

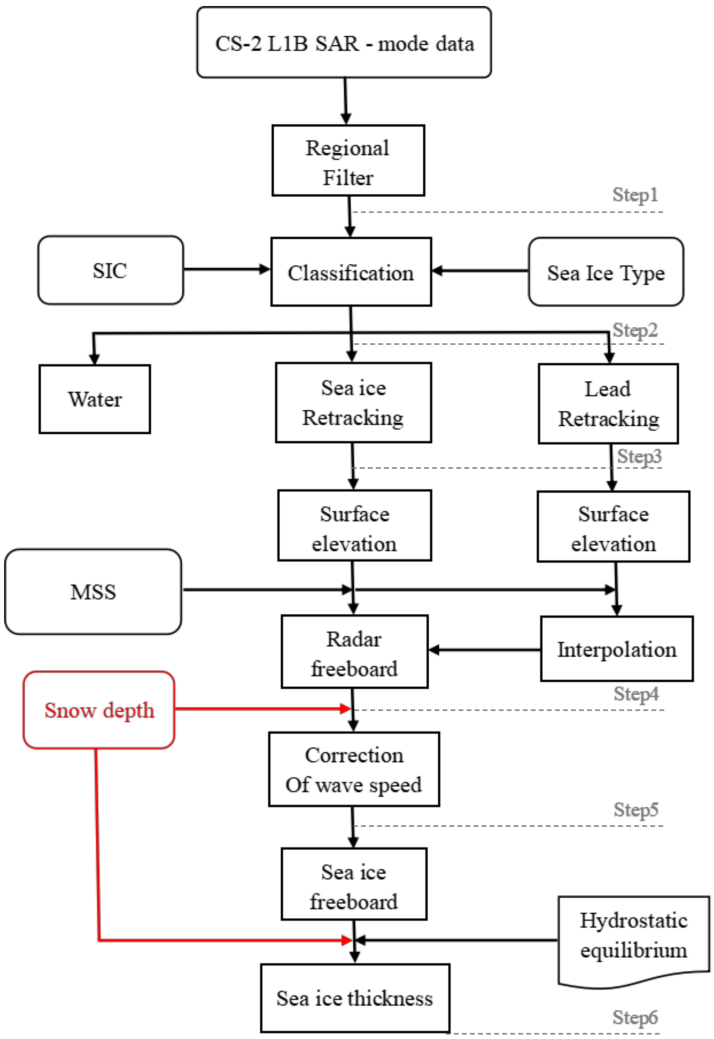

Figure 6. Flowchart of SIT retrieval.

Step 1: The data are screened to exclude the region south of 60°N.

Step 2: The effective calculation area of the sea ice freeboard is extracted with the help of SIC, and only CryoSat-2 data with SICs greater than 70% are retained to distinguish between floating ice and lead. Since the pulse signal has diffuse reflection when it reaches the surface of sea or snow and specular reflection when it reaches the lead, floating ice and the lead can be distinguished by the pulse peakiness (*PP*), standard deviation (STD) and kurtosis (K). When $PP \geq 40$, STD ≤ 4 and K ≥ 40, it is the lead; otherwise, it is the floating ice [21]. The PP value can be calculated according to Equation (13). We divide sea ice into FYI, MYI and ambiguous ice. We use only FYI and MYI data for the retrieval of sea ice freeboards.

$$PP = \frac{\max(WF_i)}{\sum_{i=1}^{256} WF_i} * 256 \quad (13)$$

where *WFi* represents the echo power at range bin index *i*.

Step 3: Due to the influence of the characteristics of the ice surface, the midpoint of the leading edge of the pulse waveform will be offset. Therefore, for the waveform of floating ice and lead, a threshold of 50% from the first-maximum peak power is used as the retracking point for retracking processing [20]. The first-maximum peak power has to be higher than the noise level by 15% of the absolute peak power, while the noise level is estimated as the average of the first five bins of the waveform [22].

Step 4: We require the leads to determine the local sea surface height. Then, by interpolating between lead tie points, we use the difference in the elevation of floating ice and the corresponding ocean surface elevation to compute the radar freeboard.

Step 5: It is assumed that electromagnetic waves can completely penetrate the snow depth. Since the speed of electromagnetic waves will attenuate when they pass through the snow layer, a wave propagation speed correction for the radar freeboard based on snow depth data is necessary [59]. According to Equation (14), the sea ice freeboard can be obtained.

$$f_i = f_r + (1 - \frac{c_s}{c}) * h_s \approx f_r + 0.22 * h_s \quad (14)$$

where c_S is the speed of light propagation through snow, c is the speed of light propagation in a vacuum, $c_S/c \approx 0.78$ [60], f_i is the sea ice freeboard, f_r is the radar freeboard and h_s is the snow depth.

Step 6: The sea ice freeboard can be converted into SIT according to Equation (15).

$$T = \frac{f_i * \rho_w + h_s * \rho_s}{\rho_w - \rho_i} \quad (15)$$

where T is the SIT; ρ_w is the density of seawater, with a value of 1024 kg/m^3; ρ_S is the density of snow; and ρ_i is the density of sea ice (the density of FYI is 916.7 kg/m^3, and the density of MYI is 882 kg/m^3) [51].

4. Results and Discussion

4.1. Comparison of Different Snow Depth Products

In this section, we conduct a comparative analysis on six snow depth products and use the snow depth measured by OIB to test the performance of the LSTM algorithm. The spatial distribution of all snow depth products from November 2018 to April 2019, including the modified W99 snow depth, AWI snow depth, Bremen snow depth, Kwok snow depth, Neural Network snow depth and LSTM snow depth, are compared and analyzed. The monthly average bias and standard deviation of snow depth in winter and spring are calculated. Finally, we discuss the results of all snow depth verifications for OIB.

Figure 7 shows the spatial distribution of products with different snow depths from November 2018 to April 2019. The spatial patterns in all products are in broad agreement; that is, snow cover is thicker over the sea ice of northern Greenland and the northern Canadian Archipelago, while snow cover is thinner over the sea ice of the Eurasian marginal Sea and Baffin Bay region. Despite the consistency of the spatial pattern, the differences between different products are obvious. The temporal evolution of products with different snow depths is also different. From January 2019 to April 2019, the modified W99 and AWI products show a huge gradient change in snow depth at the boundary between FYI and MYI, which may have been affected by the correction coefficient of 0.5 over FYI and the fusion of different products and are not consistent with the actual snow distribution. The snow depth over FYI from the Bremen products is thicker than the other snow depth products in the early stage of sea ice formation (November–December). Snow depth over MYI from the Bremen products is effective in only March and April of each spring. The Kwok snow depth is generally lower than the other snow depth products. The snow depth over MYI from the neural network and LSTM snow depth products is higher than that from the other snow depth products in the early stage of sea ice formation (November–December), which is mainly due to snow depth products heavily relying on brightness temperature combinations that are sensitive to the presence of MYI (i.e., 19 and 37 GHz)

might show thick snow in the presence of MYI even though no thick snow exists. This is also a difficult problem in the retrieval of snow depth over MYI by microwave radiometers. Moreover, snow depth products using brightness temperature (combinations) sensitive to surface roughness might also show thick snow in regions where ice is actually deformed but snow depth is not yet thick [61]. Note that it is very likely that snow depth products relying on methods such as deep learning or neural networks might appear to show snow depths thicker than the saturation snow depth (approximately 40–50 cm).

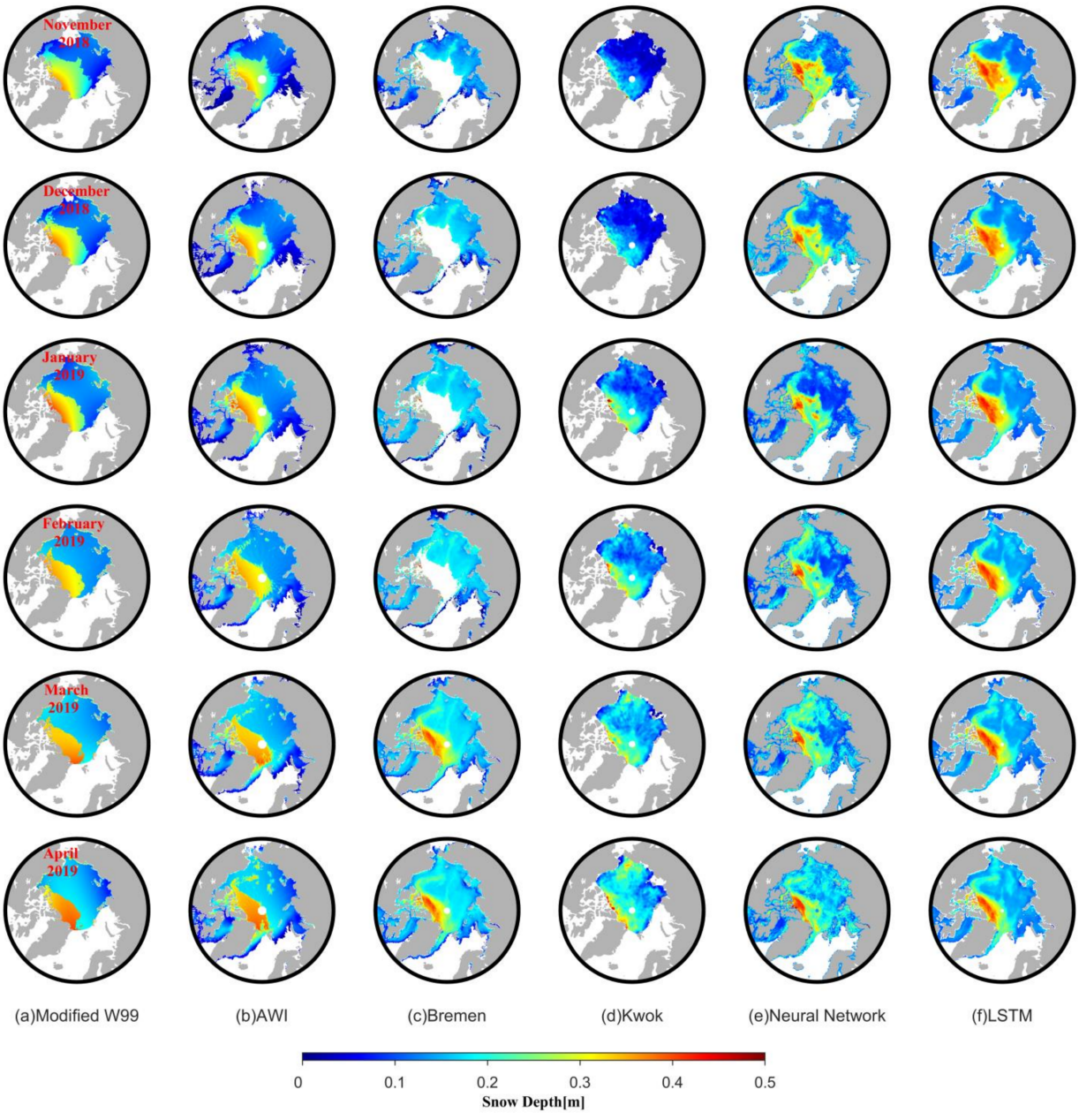

Figure 7. Spatial distribution of different snow depth products: (**a**) modified W99 snow depth, (**b**) AWI snow depth, (**c**) Bremen snow depth, (**d**) Kwok snow depth, (**e**) Neural Network snow depth, (**f**) LSTM snow depth. The dates from the first row to the last row are November 2018, December 2018, January 2019, February 2019, March 2019 and April 2019.

Figure 8 shows a bar chart of seasonal variations in snow depth over the common area of all data sets. As shown in Figure 8a, seasonal variation trends of products with different snow depths are also different. The climatology snow depth products, such as modified

W99 and AWI, show a slowly increasing trend from winter to spring. The Kwok snow depth gradually increased over time, and the snow accumulation was the largest with respect to other products. The Kwok snow depth has the lowest snow depth among all of the products. The snow accumulation time mainly occurred from December 2018 to January 2019 [41]. However, the other snow depth products fluctuated gently over time. The neural network and LSTM snow depth also showed thicker snow in early winter, decreasing first and then increasing over time. In addition, the differences in all snow depth products are relatively large in early winter and relatively small in spring. As seen from Figure 8b, the modified W99, AWI, Bremen, Kwok and LSTM show a trend of gradual accumulation over FYI. The Bremen snow depth product is larger than the other products over FYI.

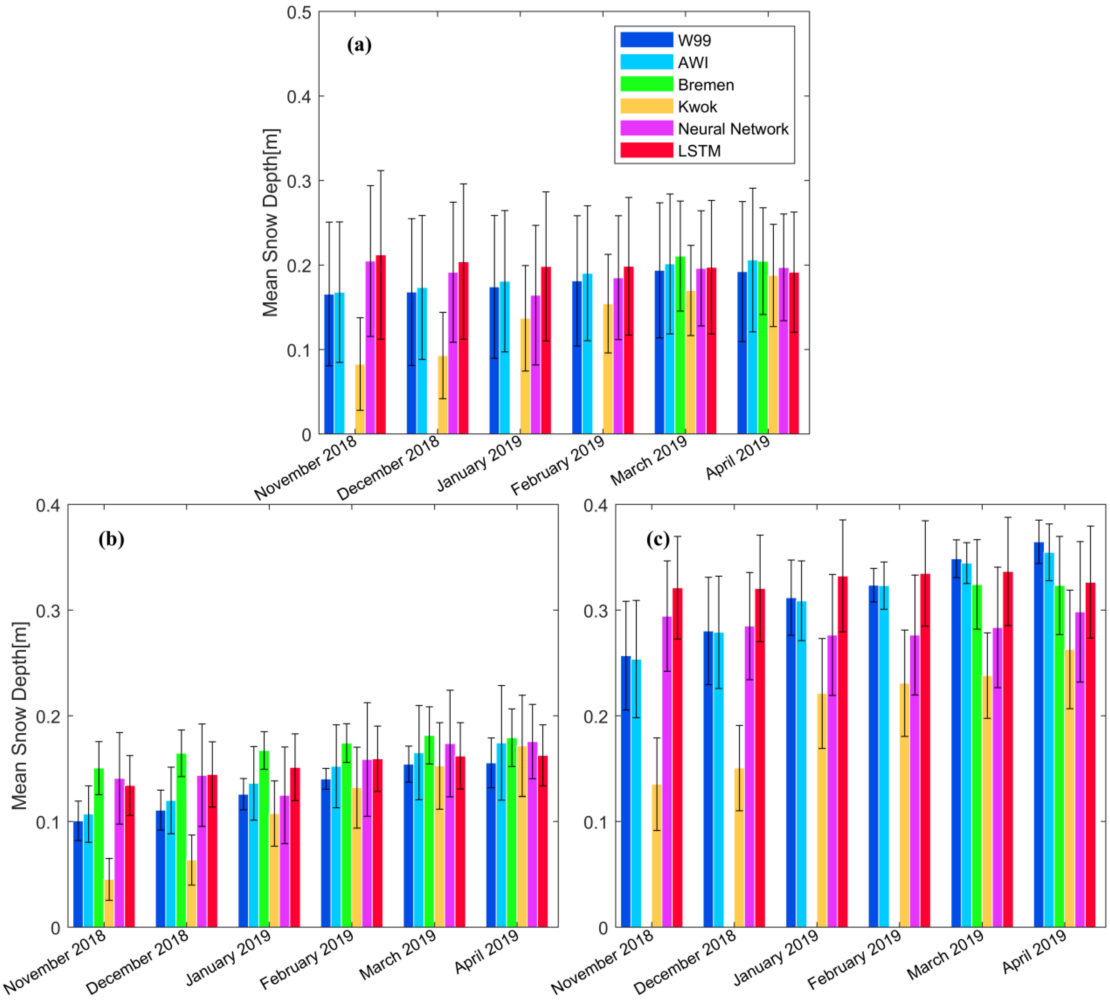

Figure 8. Histogram of seasonal variations in the different snow depth products over the common area of all data sets: (**a**) snow depth on total sea ice, (**b**) snow depth on FYI, (**c**) snow depth on MYI.

Figure 8c shows that the snow depth products of the modified W99, AWI and Kwok over the years show a gradual accumulation trend, but the snow depth products of the neural network and LSTM show a gentle trend on the seasonal curve, which is mainly limited by the retrieval accuracy of snow depth over MYI in early winter. The seasonal change trend of snow depth on MYI is consistent with the changing trend of snow depth on total ice. By comparing Figure 8b,c, it can be seen that the σ of snow depth over FYI is generally lower than that of snow depth over MYI. Table 2 summarizes the seasonal variations in different snow depth products over the common area of all data sets.

Table 2. Statistical table of the seasonal variations in the different snow depth products over the common area of all data sets.

		Gridded Mean ± Standard Deviation/Unit: m					
		Modified W99	**AWI**	**Bremen**	**Kwok**	**Neural Network**	**LSTM**
November 2018	ALL	0.17 ± 0.09	0.17 ± 0.08	/	0.08 ± 0.06	0.20 ± 0.09	0.21 ± 0.10
	FYI	0.10 ± 0.02	0.11 ± 0.03	0.15 ± 0.03	0.05 ± 0.02	0.14 ± 0.04	0.13 ± 0.03
	MYI	0.26 ± 0.05	0.25 ± 0.06	/	0.14 ± 0.04	0.29 ± 0.05	0.32 ± 0.05
December 2018	ALL	0.17 ± 0.09	0.17 ± 0.09	/	0.09 ± 0.05	0.19 ± 0.08	0.20 ± 0.09
	FYI	0.11 ± 0.02	0.12 ± 0.03	0.16 ± 0.02	0.06 ± 0.02	0.14 ± 0.05	0.14 ± 0.03
	MYI	0.28 ± 0.05	0.28 ± 0.05	/	0.15 ± 0.04	0.29 ± 0.05	0.32 ± 0.05
January 2019	ALL	0.17 ± 0.08	0.18 ± 0.08	/	0.14 ± 0.06	0.16 ± 0.08	0.20 ± 0.09
	FYI	0.13 ± 0.01	0.14 ± 0.03	0.17 ± 0.02	0.11 ± 0.03	0.13 ± 0.05	0.15 ± 0.03
	MYI	0.31 ± 0.04	0.31 ± 0.04	/	0.22 ± 0.05	0.28 ± 0.06	0.33 ± 0.05
February 2019	ALL	0.18 ± 0.08	0.19 ± 0.08	/	0.15 ± 0.06	0.19 ± 0.07	0.20 ± 0.08
	FYI	0.14 ± 0.01	0.15 ± 0.04	0.17 ± 0.02	0.13 ± 0.04	0.16 ± 0.05	0.16 ± 0.03
	MYI	0.32 ± 0.02	0.32 ± 0.02	/	0.23 ± 0.05	0.28 ± 0.06	0.33 ± 0.05
March 2019	ALL	0.19 ± 0.08	0.20 ± 0.08	0.21 ± 0.07	0.17 ± 0.05	0.20 ± 0.07	0.20 ± 0.08
	FYI	0.15 ± 0.02	0.17 ± 0.04	0.18 ± 0.03	0.15 ± 0.04	0.17 ± 0.05	0.16 ± 0.03
	MYI	0.35 ± 0.02	0.34 ± 0.02	0.32 ± 0.04	0.24 ± 0.04	0.28 ± 0.06	0.34 ± 0.05
April 2019	ALL	0.19 ± 0.08	0.21 ± 0.09	0.20 ± 0.06	0.19 ± 0.06	0.20 ± 0.06	0.19 ± 0.07
	FYI	0.16 ± 0.02	0.17 ± 0.05	0.18 ± 0.03	0.17 ± 0.05	0.18 ± 0.04	0.16 ± 0.03
	MYI	0.36 ± 0.02	0.35 ± 0.03	0.32 ± 0.05	0.26 ± 0.06	0.30 ± 0.07	0.33 ± 0.05

We added all snow depth products and snow depths measured by OIB into a 25 km grid to evaluate the various snow depth products in April 2019, as shown in Figure 9. The RMSE and (mean absolute error) MAE values of LSTM are 0.05 and 0.06 m, respectively, which are lower than those of the other snow depth products excluding the Bremen snow depth product and have a high correlation of 0.55, second only to that of the Kwok snow depth (correlation of 0.62). This indicates that the deep learning algorithm of LSTM is suitable. Figure 9a,b shows that the modified W99 and AWI snow depths are stratified at the boundary between FYI and MYI, which is mainly affected by the correction coefficient of 0.5 over FYI. Compared with the snow depth measurement from OIB, the correlations of modified W99 and AWI are 0.19 and 0.28, respectively, and the RMSEs are 0.09 and 0.08 m, respectively. Figure 9d shows that the snow depth from Kwok is lower than that from OIB, while the correlation between the snow depth from Kwok and OIB is the highest. Figure 9e shows that the correlation between the neural network and OIB snow depths is 0.26, the RMSE is 0.09 m and the accuracy is lower than that of the LSTM and Bremen snow depth.

We also used IceBird observation data, which is completely independent of OIB data, to verify six snow depth products, as shown in Figure 10. We set the minimum number of observation points as 50 in all of the validations of snow depth to reduce the effect of limit representation of OIB and IceBird. The LSTM has the best snow depth retrieval performance, with the highest correlation of 0.90, the lowest RMSE of 0.05 m and the lowest MAE of 0.04 m. This also indicates that the LSTM algorithm is effective and feasible in retrieving Arctic snow depth. Furthermore, we found that the correlation coefficient of IceBird validation is higher than OIB validation. This is mainly because the number of measurement points of IceBird (approximately 4500) in each grid after gridding is more than that of OIB (approximately 450), and the footprint of IceBird is smaller than that of OIB, resulting in a more uniform distribution of IceBird in each grid. Therefore, the grid data of IceBird is more representative than OIB.

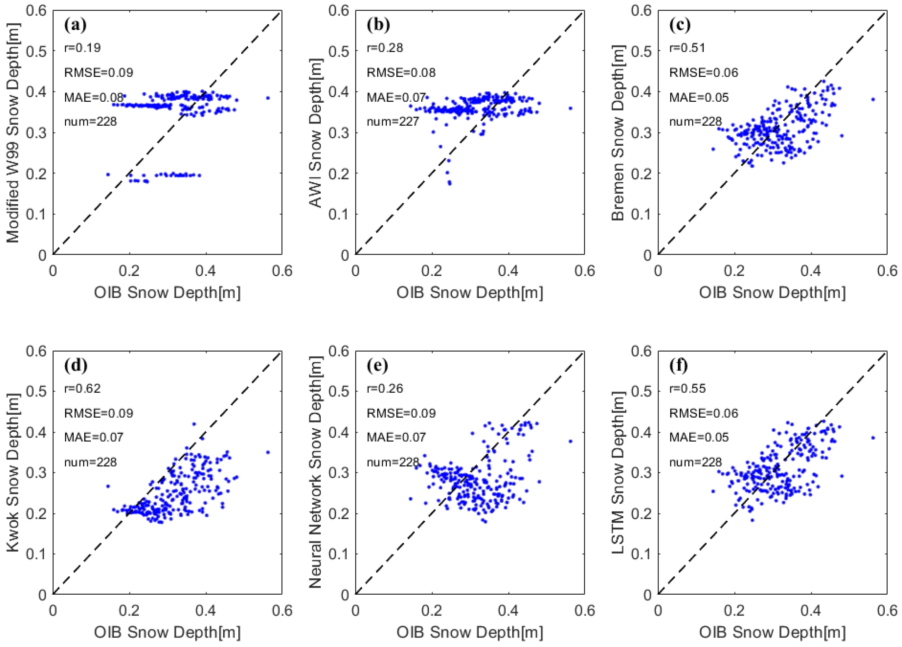

Figure 9. Scatterplots of different snow depth products and OIB snow depth: (**a**) modified W99 snow depth, (**b**) AWI snow depth, (**c**) Bremen snow depth, (**d**) Kwok snow depth, (**e**) Neural Network snow depth, (**f**) LSTM snow depth. The black line is the relationship with each other.

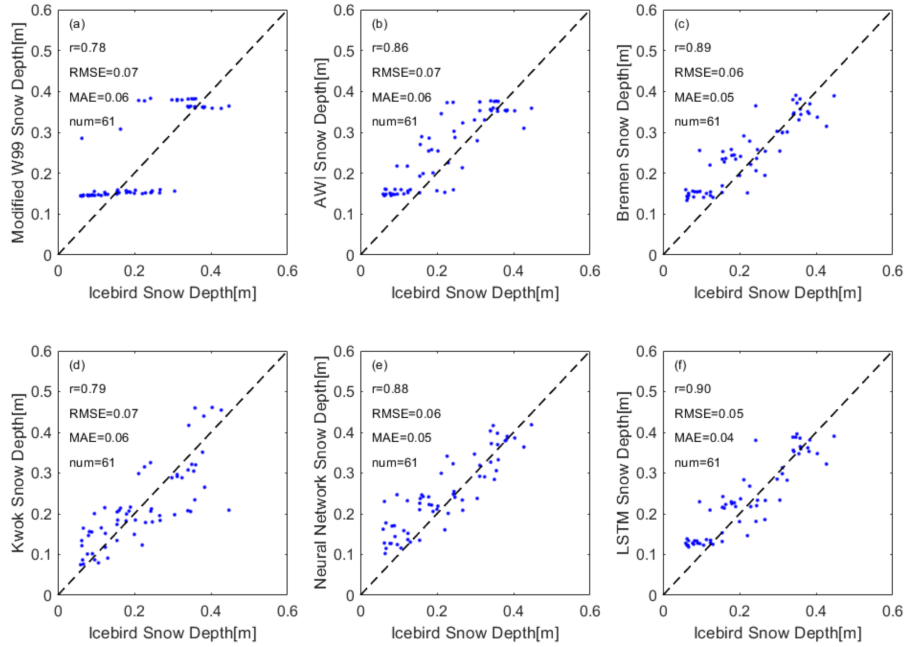

Figure 10. Scatterplots of different snow depth products and IceBird snow depth: (**a**) modified W99 snow depth, (**b**) AWI snow depth, (**c**) Bremen snow depth, (**d**) Kwok snow depth, (**e**) Neural Network snow depth, (**f**) LSTM snow depth. The black line is the relationship with each other.

4.2. Comparison of the SITs Retrieved from Different Snow Depth Products

In this section, we retrieve the SIT in the Arctic region from November 2018 to April 2019 based on the Cryosat-2 radar altimeter and the six snow depth products mentioned above. We perform a comparative analysis on the SIT retrieved by the six snow depth products. We calculate the monthly average and standard deviation of the SIT from various

snow depth products in winter and spring. Finally, we verify the retrieval of SIT with the OIB SIT.

Figure 11 shows the spatial distribution of SIT retrieved from different snow depth products during winter and spring. The spatial patterns of all SIT products are in broad agreement; thicker sea ice occurs north of Greenland, north of the Canadian Archipelago and the central Arctic area, with thinner sea ice in the Eurasian continental marginal sea and Baffin Bay, which is mainly affected by the influence of large-scale atmospheric circulation (prevailing winds) on sea ice motion, with the atmospheric Beaufort High driving the counterclockwise (anticyclonic) movement of sea ice in the Beaufort Gyre [62]. As a result, Arctic Ocean sea ice converges against the northern coasts of Greenland and the CAA, creating some of the thickest sea ice in the world, with some floes over 5 m thick [25]. All the results reveal that the Arctic sea ice thickens with the seasons, especially in the FYI region. Despite the consistency of the spatial pattern and temporal variation, there are significant differences between the SIT products in the same month. The SIT retrieved from the Kwok snow depth is the smallest among all the SIT products because the Kwok snow depth is shallower than the other products. The FYI retrieved from the Bremen snow depth is the largest with respect to other products because the Bremen snow depth over FYI is thicker than the other products. However, in early winter (November–December), the MYI thicknesses from the neural network and LSTM are larger than those of the other SIT products, mainly due to the deeper snow depths over the MYI from the neural network and LSTM in early winter.

Figure 12 shows the seasonal variation in the monthly average Arctic SIT over the common area of all data sets. All SIT products, excluding Bremen retrieval, first decrease and then increase over time, which is mainly affected by the trends of sea ice freeboard and snow depth. The SIT from the Bremen snow depth retrieval also gradually increases from March to April. The SIT of Kwok snow depth retrieval shows that the thickness accumulation of all products is the largest, followed by the SITs retrieved by climatological snow depth products, and the SITs retrieved by neural network and LSTM are the smallest. The differences in all SIT products are relatively large in early winter and relatively small in spring which mainly results from the differences in all snow depth products. The thicknesses from all sea ice products increase for FYI (see Figure 12b). Figure 12c shows that all SIT products reveal an increasing trend for MYI from January to April while showing a slowly decreasing trend from November to December, except for the SIT retrieved by Bremen. The seasonal change trend of MYI is consistent with the total sea ice. Table 3 shows the statistical table of the seasonal variations in different Arctic SIT products over the common area of all data sets.

The radar freeboard measured by CryoSat-2 is combined with six snow depth products to conduct wave speed correction. Sea ice freeboard can be converted to SIT by using hydrostatic equilibrium combined with six snow depth products, which can be grided into 25 km monthly average SIT data for verification with OIB SIT, as shown in Figure 13. We set the minimum number of observation points as 50 in all of the validations of SIT to reduce the effect of limit representation of OIB. The results show that the LSTM has the best SIT retrieval performance, with the highest correlation of 0.46, the lowest RMSE of 0.59 m and the lowest MAE of 0.44 m. This shows that the LSTM algorithm can not only retrieve snow depth with high precision but also its corresponding snow products to improve the accuracy of SIT retrieval.

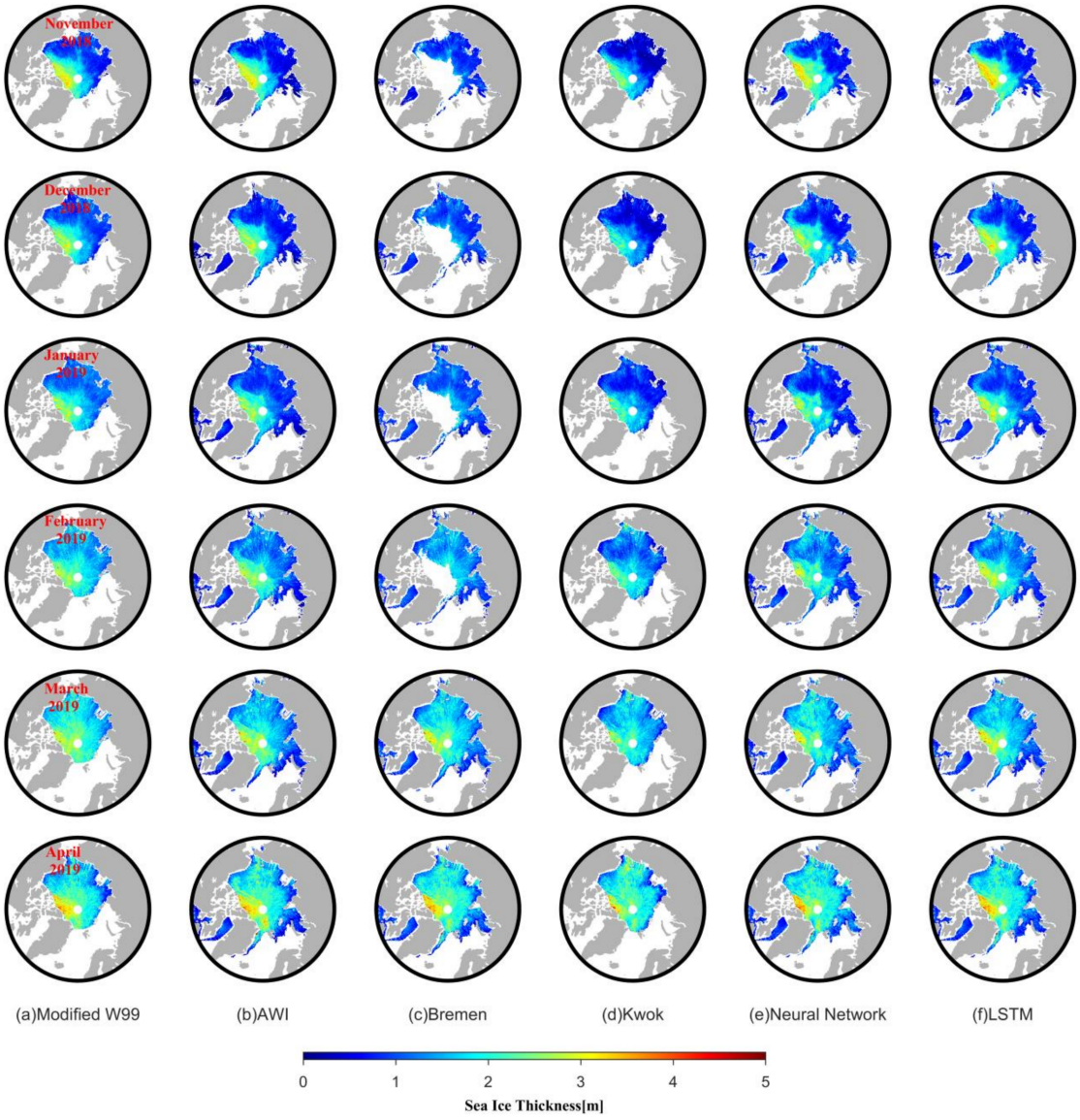

Figure 11. Spatial distribution of SIT from different snow depth product retrievals: (**a**) modified W99 snow depth, (**b**) AWI snow depth, (**c**) Bremen snow depth, (**d**) Kwok snow depth, (**e**) Neural Network snow depth and (**f**) LSTM snow depth. The dates from the first row to the last row are November 2018, December 2018, January 2019, February 2019, March 2019 and April 2019.

Table 3. Statistical table of the seasonal variations in different Arctic SIT products over the common area of all data sets.

		Gridded Mean ± Standard Deviation/Unit: m					
		Modified W99	**AWI**	**Bremen**	**Kwok**	**Neural Network**	**LSTM**
November 2018	ALL	1.30 ± 0.81	1.31 ± 0.81	/	0.97 ± 0.72	1.46 ± 0.80	1.48 ± 0.86
	FYI	0.74 ± 0.28	0.76 ± 0.31	0.95 ± 0.31	0.48 ± 0.31	0.91 ± 0.37	0.88 ± 0.33
	MYI	2.10 ± 0.63	2.11 ± 0.62	/	1.69 ± 0.53	2.26 ± 0.53	2.36 ± 0.59
December 2018	ALL	1.23 ± 0.68	1.25 ± 0.68	/	0.93 ± 0.59	1.34 ± 0.67	1.38 ± 0.71
	FYI	0.84 ± 0.30	0.87 ± 0.33	1.07 ± 0.33	0.62 ± 0.33	0.98 ± 0.42	0.98 ± 0.36
	MYI	2.02 ± 0.54	2.03 ± 0.52	/	1.57 ± 0.45	2.06 ± 0.45	2.19 ± 0.52
January 2019	ALL	1.28 ± 0.59	1.31 ± 0.60	/	1.13 ± 0.55	1.24 ± 0.62	1.39 ± 0.63
	FYI	0.99 ± 0.28	1.03 ± 0.33	1.16 ± 0.32	0.90 ± 0.36	0.97 ± 0.41	1.10 ± 0.36
	MYI	2.09 ± 0.49	2.11 ± 0.46	/	1.78 ± 0.46	1.99 ± 0.48	2.20 ± 0.52

Table 3. *Cont.*

		Gridded Mean ± Standard Deviation/Unit: m					
		Modified W99	**AWI**	**Bremen**	**Kwok**	**Neural Network**	**LSTM**
February 2019	ALL	1.50 ± 0.54	1.54 ± 0.56	/	1.39 ± 0.52	1.53 ± 0.55	1.58 ± 0.58
	FYI	1.29 ± 0.34	1.33 ± 0.40	1.42 ± 0.37	1.24 ± 0.43	1.36 ± 0.44	1.37 ± 0.40
	MYI	2.23 ± 0.44	2.28 ± 0.41	/	1.92 ± 0.45	2.10 ± 0.49	2.32 ± 0.50
March 2019	ALL	1.72 ± 0.53	1.76 ± 0.55	1.81 ± 0.53	1.64 ± 0.49	1.75 ± 0.52	1.74 ± 0.56
	FYI	1.53 ± 0.37	1.57 ± 0.42	1.65 ± 0.41	1.52 ± 0.44	1.62 ± 0.44	1.56 ± 0.40
	MYI	2.46 ± 0.40	2.50 ± 0.38	2.42 ± 0.48	2.08 ± 0.42	2.26 ± 0.51	2.46 ± 0.51
April 2019	ALL	1.93 ± 0.62	1.99 ± 0.63	1.99 ± 0.58	1.92 ± 0.57	1.96 ± 0.57	1.93 ± 0.60
	FYI	1.75 ± 0.47	1.83 ± 0.52	1.85 ± 0.47	1.82 ± 0.53	1.84 ± 0.45	1.77 ± 0.46
	MYI	2.79 ± 0.51	2.77 ± 0.50	2.66 ± 0.60	2.40 ± 0.54	2.56 ± 0.65	2.67 ± 0.62

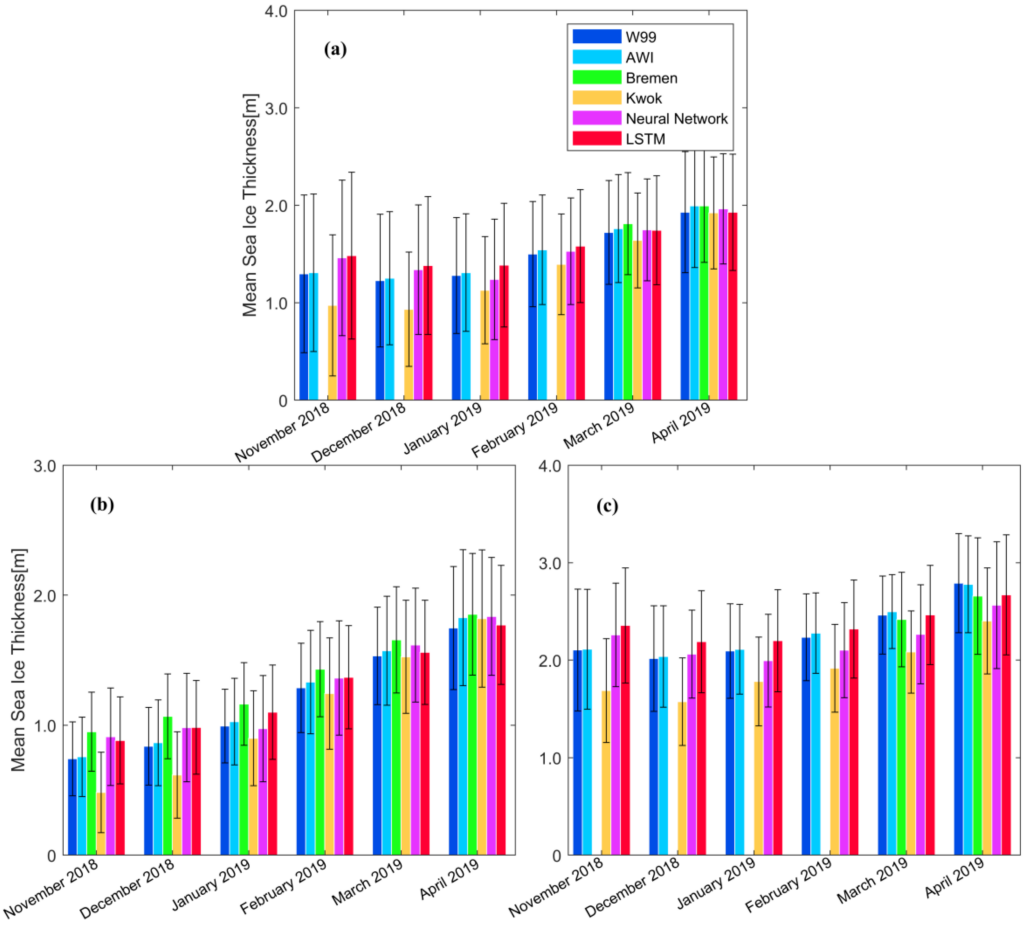

Figure 12. Histogram of seasonal variations in different SIT products: (**a**) total sea ice, (**b**) FYI and (**c**) MYI.

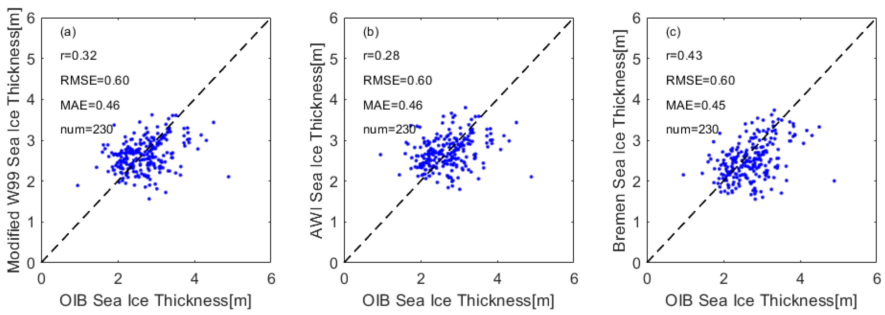

Figure 13. *Cont.*

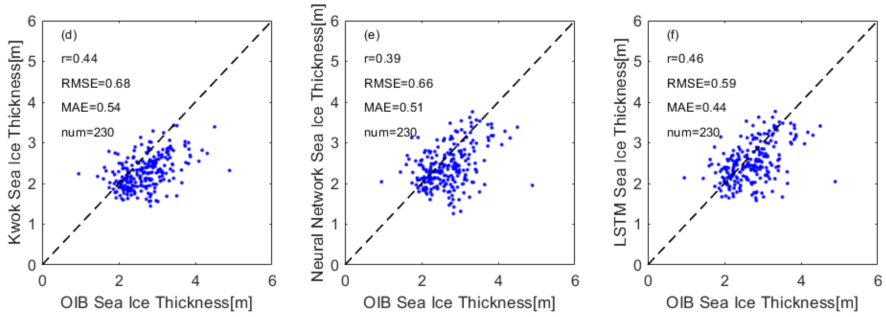

Figure 13. Evaluation of the CryoSat-2 (CS-2) SIT retrieved from different snow depths compared with the OIB sea ice thickness: (**a**) modified W99 snow depth, (**b**) AWI snow depth, (**c**) Bremen snow depth, (**d**) Kwok snow depth, (**e**) Neural Network snow depth and (**f**) LSTM snow depth. The black line is the relationship with each other.

5. Conclusions

In this study, we developed an Arctic snow depth retrieval model with an LSTM deep learning algorithm based on the brightness temperature measurements of the AMSR-2 microwave radiometer and OIB snow depth data from 2013 to 2018. The established model was validated by the measurements of snow depth of OIB and IceBird in April 2019 and compared with the modified W99, AWI, Bremen, Kwok and Neural Network snow depth products. The above six snow depth products were used to retrieve SIT based on CryoSat-2 radar altimeter data. We compared the SIT products retrieved from different snow depth products and used the OIB SIT in April 2019 for validation analysis. The main conclusions are as follows.

The spatial distribution of snow depth obtained by the different data sources and algorithms is consistent in that the snow depth on the sea ice of northern Greenland and the northern part of the Canadian Archipelago is thicker while the snow depth on the sea ice of the Eurasian marginal Sea and Baffin Bay is thinner. Despite the consistency of the spatial pattern, the differences among different products are obvious. The temporal evolution of snow depth also varies with different products. During the winter and spring periods (from November 2018 to April 2019), the modified W99 snow depth ranges from 0.17 to 0.19 m. The AWI snow depth ranges from 0.17 to 0.21 m. The climatology snow depth products show a slowly increasing trend from winter to spring. The Kwok snow depth ranges from 0.08 to 0.19 m. The altimeter product of KWOK snow depth shows a significantly increasing trend with the largest snow accumulation. The range of snow depth from the neural network is 0.20 to 0.20 m with a gentle fluctuation from November 2018 to April 2019, and the LSTM snow depth range is 0.21 to 0.19 m with a decreasing trend from November 2018 to April 2019. Snow products of microwave radiometers, such as Bremen, Neural Network and LSTM snow depth products, show thicker snow in early winter with respect to the climatology snow depth products and the altimeter product of KWOK snow depth, especially in the MYI region. In addition, the differences in all snow depth products are relatively large in the early winter and relatively small in spring. Finally, the verification with OIB snow depth shows that the LSTM algorithm is better than the other algorithms at snow depth retrieval in terms of accuracy; its correlation is 0.55, its RMSE is 0.06 m and its MAE is 0.05 m. The validation from the IceBird observation data, which is completely independent of OIB, also shows that the LSTM has the best snow depth retrieval performance, with the highest correlation of 0.90, the lowest RMSE of 0.05 m and the lowest MAE of 0.04 m.

The spatial distribution and seasonal variation in the SIT from different snow depth product retrievals are basically consistent. The SIT in the northern part of Greenland and the northern part of the Canadian Archipelago is thicker, while the SIT in the Eurasian marginal Sea and Baffin Bay is thinner. All the results indicate that Arctic sea ice decreases first and then thickens as the seasons change. In addition, the FYI thickens as the seasons change. However, seasonal variations in different SIT products also vary significantly. The

SIT from the modified W99 retrieval ranges from 1.30 to 1.93 m. The SIT derived from the AWI ranges from 1.31 to 1.99 m. The SIT retrieved by the climatology snow products shows a slowly increasing trend from winter to spring. The SIT from the Kwok snow depth retrieval ranges from 0.97 to 1.92 m with the largest thickness accumulation. The range of SITs derived from the neural network snow depth retrieval is 1.46 to 1.96 m. The range of SITs retrieved from the LSTM snow depth is 1.48 to 1.93 m. Ice thickness products retrieved from microwave radiometer snow products are both thicker in early winter with respect to other products, especially in the MYI region. The differences in all SIT products are relatively large in early winter and relatively small in spring, which mainly results from the differences in all snow depth products. Verification with OIB SIT indicates that the LSTM SIT retrieval is better than the SIT retrieval of the other products in terms of accuracy, with the highest correlation of 0.46, the lowest RMSE of 0.59 m and the lowest MAE of 0.44 m.

In general, it is promising to retrieve Arctic snow depth using the LSTM algorithm. At present, there is a lack of relevant verification data for snow depth retrieval and SIT retrieval in early winter since the limited field survey data and the low-temporal-resolution OIB airborne data are mainly concentrated in March and April. In future studies, we will collect more field survey data and conduct a more systematic comparison and verification of different snow depth products and SIT products.

Author Contributions: Data curation, Z.D. and L.S.; writing, Z.D. and L.S.; methodology, Z.D., L.S., M.L. and T.Z.; validation, Z.D. and T.Z.; funding acquisition, L.S. and M.L. All authors have read and agreed to the published version of the manuscript.

Funding: This research was funded by the National Key Research and Development Program of China grant numbers 2018YFC1407200, 2018YFC1407206 and IRASCC2020-2022-No.01-01-03.

Institutional Review Board Statement: Not applicable.

Informed Consent Statement: Not applicable.

Data Availability Statement: The AMSR-2 brightness temperature data can be requested from the University of Bremen (https://seaice.uni-bremen.de/data/amsr2/tb_daygrid_swath/, accessed on 25 September 2021). The SAR mode L1B data for CryoSat-2 (CS-2) can be requested from the European Space Agency (ESA) (https://science-pds.cryosat.esa.int/, accessed on 25 September 2021). The IceBridge IDCSI4 data can be requested from NSIDC (https://nsidc.org/data/NSIDC-0708/versions/1/, accessed on 25 September 2021). The IceBird data can be requested from PANGAEA (https://doi.pangaea.de/10.1594/PANGAEA.932790/, accessed on 25 September 2021). The W99 climatology snow depth product and the AWI snow depth product can be requested from the Alfred Wegener Institute (AWI) (https://data.seaiceportal.de/gallery/index_new.php?lang=en_US/, accessed on 25 September 2021). The Bremen snow depth product can be requested from the University of Bremen (https://seaice.uni-bremen.de/data/amsr2/SnowDepth/n25000/, accessed on 25 September 2021). The Kwok snow depth product can be downloaded from the website (https://doi.pangaea.de/10.1594/PANGAEA.914565?format=html#download/, accessed on 25 September 2021). Sea ice type and sea ice concentration data can be requested from the Ocean and Sea Ice Satellite Application Facility (https://osi-saf.eumetsat.int/, accessed on 25 September 2021). The DTU18 MSS data can be requested from the Technical University of Denmark (ftp://ftp.space.dtu.dk/pub/, accessed on 25 September 2021).

Acknowledgments: We would like to thank the University of Bremen, ESA, NSIDC, AWI, OSI-SAF and DTU for providing all the data needed for this paper.

Conflicts of Interest: The authors declare no conflict of interest.

References

1. Dai, A.; Luo, D.; Song, M.; Liu, J. Arctic amplification is caused by sea-ice loss under increasing CO2. *Nat. Commun.* **2019**, *10*, 121. [CrossRef] [PubMed]
2. Comiso, J.C.; Parkinson, C.; Gersten, R.; Stock, L. Accelerated decline in the Arctic sea ice cover. *Geophys. Res. Lett.* **2008**, *35*, 01703. [CrossRef]
3. Kwok, R. Arctic sea ice thickness, volume, and multiyear ice coverage: Losses and coupled variability (1958–2018). *Environ. Res. Lett.* **2018**, *13*, 105005. [CrossRef]

4. Lindsay, R.; Schweiger, A. Arctic sea ice thickness loss determined using subsurface, aircraft, and satellite observations. *Cryosphere* **2015**, *9*, 269–283. [CrossRef]
5. Kurtz, N.T.; Markus, T.; Farrell, S.; Worthen, D.L.; Boisvert, L.N. Observations of recent Arctic sea ice volume loss and its impact on ocean-atmosphere energy exchange and ice production. *J. Geophys. Res. Earth Surf.* **2011**, *116*, 04015. [CrossRef]
6. Perovich, D.; Jones, K.; Light, B.; Eicken, H.; Markus, T.; Stroeve, J.; Lindsay, R. Solar partitioning in a changing Arctic sea-ice cover. *Ann. Glaciol.* **2011**, *52*, 192–196. [CrossRef]
7. Perovich, D.K.; Grenfell, T.C.; Light, B.; Hobbs, P.V. Seasonal evolution of the albedo of multiyear Arctic sea ice. *J. Geophys. Res. Earth Surf.* **2002**, *107*, SHE 20-1–SHE 20-13. [CrossRef]
8. Sturm, M.; Perovich, D.K.; Holmgren, J. Thermal conductivity and heat transfer through the snow on the ice of the Beaufort Sea. *J. Geophys. Res. Earth Surf.* **2002**, *107*, SHE 19-1–SHE 19-17. [CrossRef]
9. Liu, J.; Zhang, Y.; Cheng, X.; Hu, Y. Retrieval of Snow Depth over Arctic Sea Ice Using a Deep Neural Network. *Remote Sens.* **2019**, *11*, 2864. [CrossRef]
10. Fichefet, T.; Maqueda, M.A.M. Modelling the influence of snow accumulation and snow-ice formation on the seasonal cycle of the Antarctic sea-ice cover. *Clim. Dyn.* **1999**, *15*, 251–268. [CrossRef]
11. Perovich, D.; Polashenski, C.; Arntsen, A.; Stwertka, C. Anatomy of a late spring snowfall on sea ice. *Geophys. Res. Lett.* **2017**, *44*, 2802–2809. [CrossRef]
12. Schröder, D.; Feltham, D.L.; Flocco, D.; Tsamados, M. September Arctic sea-ice minimum predicted by spring melt-pond fraction. *Nat. Clim. Change* **2014**, *4*, 353–357. [CrossRef]
13. Liu, J.; Song, M.; Horton, R.M.; Hu, Y. Revisiting the potential of melt pond fraction as a predictor for the seasonal Arctic sea ice extent minimum. *Environ. Res. Lett.* **2015**, *10*, 054017. [CrossRef]
14. Laxon, S.; Peacock, N.; Smith, D. High interannual variability of sea ice thickness in the Arctic region. *Nature* **2003**, *425*, 947–950. [CrossRef] [PubMed]
15. Paul, S.; Hendricks, S.; Ricker, R.; Kern, S.; Rinne, E. Empirical parametrization of Envisat freeboard retrieval of Arctic and Antarctic sea ice based on CryoSat-2: Progress in the ESA Climate Change Initiative. *Cryosphere* **2018**, *12*, 2437–2460. [CrossRef]
16. Giles, K.; Laxon, S.; Wingham, D.; Wallis, D.; Krabill, W.; Leuschen, C.; McAdoo, D.; Manizade, S.; Raney, R. Combined airborne laser and radar altimeter measurements over the Fram Strait in May 2002. *Remote Sens. Environ.* **2007**, *111*, 182–194. [CrossRef]
17. Zygmuntowska, M.; Rampal, P.; Ivanova, N.; Smedsrud, L.H. Uncertainties in Arctic sea ice thickness and volume: New estimates and implications for trends. *Cryosphere* **2014**, *8*, 705–720. [CrossRef]
18. Kwok, R.; Zwally, H.J.; Yi, D. ICESat observations of Arctic sea ice: A first look. *Geophys. Res. Lett.* **2004**, *31*, 16401. [CrossRef]
19. Giles, K.A.; Laxon, S.W.; Ridout, A.L. Circumpolar thinning of Arctic sea ice following the 2007 record ice extent minimum. *Geophys. Res. Lett.* **2008**, *35*, L22502. [CrossRef]
20. Laxon, S.W.; Giles, K.A.; Ridout, A.L.; Wingham, D.J.; Willatt, R.; Cullen, R.; Kwok, R.; Schweiger, A.; Zhang, J.; Haas, C.; et al. CryoSat-2 estimates of Arctic sea ice thickness and volume. *Geophys. Res. Lett.* **2013**, *40*, 732–737. [CrossRef]
21. Ricker, R.; Hendricks, S.; Helm, V.; Skourup, H.; Davidson, M. Sensitivity of CryoSat-2 Arctic sea-ice freeboard and thickness on radar-waveform interpretation. *Cryosphere* **2014**, *8*, 1607–1622. [CrossRef]
22. Tilling, R.L.; Ridout, A.; Shepherd, A. Near-real-time Arctic sea ice thickness and volume from CryoSat-2. *Cryosphere* **2016**, *10*, 2003–2012. [CrossRef]
23. Warren, S.G.; Rigor, I.G.; Untersteiner, N.; Radionov, V.F.; Bryazgin, N.N.; Aleksandrov, Y.I.; Colony, R. Snow Depth on Arctic Sea Ice. *J. Clim.* **1999**, *12*, 1814–1829. [CrossRef]
24. Kurtz, N.T.; Farrell, S. Large-scale surveys of snow depth on Arctic sea ice from Operation IceBridge. *Geophys. Res. Lett.* **2011**, *38*, 20. [CrossRef]
25. Kwok, R.; Cunningham, G.F. Variability of Arctic sea ice thickness and volume from CryoSat-2. *Philos. Trans. R. Soc. London Ser. A Math. Phys. Eng. Sci.* **2015**, *373*, 20140157. [CrossRef] [PubMed]
26. Webster, M.A.; Rigor, I.G.; Nghiem, S.V.; Kurtz, N.T.; Farrell, S.L.; Perovich, D.K.; Sturm, M. Interdecadal changes in snow depth on Arctic sea ice. *J. Geophys. Res. Oceans* **2014**, *119*, 5395–5406. [CrossRef]
27. Kern, S.; Khvorostovsky, K.; Skourup, H.; Rinne, E.; Parsakhoo, Z.S.; Djepa, V.; Wadhams, P.; Sandven, S. The impact of snow depth, snow density and ice density on sea ice thickness retrieval from satellite radar altimetry: Results from the ESA-CCI Sea Ice ECV Project Round Robin Exercise. *Cryosphere* **2015**, *9*, 37–52. [CrossRef]
28. Markus, T.; Cavalieri, D.J. Snow Depth Distribution Over Sea Ice in the Southern Ocean from Satellite Passive Microwave Data, Antarctic Sea Ice: Physical Processes, Interactions and Variability. *Antarct. Res. Ser.* **1998**, *74*, 19–39. [CrossRef]
29. Comiso, J.; Cavalieri, D.; Markus, T. Sea ice concentration, ice temperature, and snow depth using AMSR-E data. *IEEE Trans. Geosci. Remote Sens.* **2003**, *41*, 243–252. [CrossRef]
30. Meier, W.N.; Markus, T.; Comiso, J.C. *AMSR-E/AMSR2 Unified L3 Daily 12.5 km Brightness Temperatures, Sea Ice Concentration, Motion & Snow Depth Polar Grids, Version 1*; NASA National Snow and Ice Data Center Distributed Active Archive Center: Boulder, CO, USA, 2018. [CrossRef]
31. Markus, T.; Powell, D.; Wang, J. Sensitivity of passive microwave snow depth retrievals to weather effects and snow evolution. *IEEE Trans. Geosci. Remote Sens.* **2005**, *44*, 68–77. [CrossRef]

32. Rostosky, P.; Spreen, G.; Farrell, S.L.; Frost, T.; Heygster, G.; Melsheimer, C. Snow Depth Retrieval on Arctic Sea Ice from Passive Microwave Radiometers—Improvements and Extensions to Multiyear Ice Using Lower Frequencies. *J. Geophys. Res. Oceans* **2018**, *123*, 7120–7138. [CrossRef]
33. Kilic, L.; Tonboe, R.T.; Prigent, C.; Heygster, G. Estimating the snow depth, the snow–ice interface temperature, and the effective temperature of Arctic sea ice using Advanced Microwave Scanning Radiometer 2 and ice mass balance buoy data. *Cryosphere* **2019**, *13*, 1283–1296. [CrossRef]
34. Li, L.; Chen, H.; Guan, L. Retrieval of Snow Depth on Arctic Sea Ice from the FY3B/MWRI. *Remote Sens.* **2021**, *13*, 1457. [CrossRef]
35. Braakmann-Folgmann, A.; Donlon, C. Estimating snow depth on Arctic sea ice using satellite microwave radiometry and a neural network. *Cryosphere* **2019**, *13*, 2421–2438. [CrossRef]
36. Maaß, N.; Kaleschke, L.; Tian-Kunze, X.; Drusch, M. Snow thickness retrieval over thick Arctic sea ice using SMOS satellite data. *Cryosphere* **2013**, *7*, 1971–1989. [CrossRef]
37. Zhou, L.; Xu, S.; Liu, J.; Lu, H.; Wang, B. Improving L-band radiation model and representation of small-scale variability to simulate brightness temperature of sea ice. *Int. J. Remote Sens.* **2017**, *38*, 7070–7084. [CrossRef]
38. Xu, S.; Zhou, L.; Liu, J.; Lu, H.; Wang, B. Data Synergy between Altimetry and L-Band Passive Microwave Remote Sensing for the Retrieval of Sea Ice Parameters—A Theoretical Study of Methodology. *Remote Sens.* **2017**, *9*, 1079. [CrossRef]
39. Zhou, L.; Xu, S.; Liu, J.; Wang, B. On the retrieval of sea ice thickness and snow depth using concurrent laser altimetry and L-band remote sensing data. *Cryosphere* **2018**, *12*, 993–1012. [CrossRef]
40. Guerreiro, K.; Fleury, S.; Zakharova, E.; Rémy, F.; Kouraev, A. Potential for estimation of snow depth on Arctic sea ice from CryoSat-2 and SARAL/AltiKa missions. *Remote Sens. Environ.* **2016**, *186*, 339–349. [CrossRef]
41. Kwok, R.; Kacimi, S.; Webster, M.; Kurtz, N.; Petty, A. Arctic Snow Depth and Sea Ice Thickness from ICESat-2 and CryoSat-2 Freeboards: A First Examination. *J. Geophys. Res. Oceans* **2020**, *125*, e2019JC016008. [CrossRef]
42. Du, J.; Kimball, J.S.; Shi, J.; Jones, L.A.; Wu, S.; Sun, R.; Yang, H. Inter-Calibration of Satellite Passive Microwave Land Observations from AMSR-E and AMSR2 Using Overlapping FY3B-MWRI Sensor Measurements. *Remote Sens.* **2014**, *6*, 8594–8616. [CrossRef]
43. Frederick, P.I. *Map Projections: Theory and Applications*; CRC Press: Boca Raton, FL, USA, 1990.
44. Snyder, J.P. *Map Projections—A Working Manual*; US Government Printing Office: Washington, DC, USA, 1987; Volume 1395.
45. Shi, L.; Liu, S.; Shi, Y.; Ao, X.; Zou, B.; Wang, Q. Sea Ice Concentration Products over Polar Regions with Chinese FY3C/MWRI Data. *Remote Sens.* **2021**, *13*, 2174. [CrossRef]
46. European Space Agency. CryoSat-2 Product Handbook [EB/OL]. (23-11-2020) [01-12-2020]. Available online: http://science-pds.cryosat.esa.int/ (accessed on 19 December 2021).
47. Krabill, W.B.; Thomas, R.H.; Martin, C.F.; Swift, R.N.; Frederick, E.B. Accuracy of airborne laser altimetry over the Greenland ice sheet. *Int. J. Remote Sens.* **1995**, *16*, 1211–1222. [CrossRef]
48. Kurtz, N.T.; Farrell, S.L.; Studinger, M.; Galin, N.; Harbeck, J.P.; Lindsay, R.; Onana, V.D.; Panzer, B.; Sonntag, J.G. Sea ice thickness, freeboard, and snow depth products from Operation IceBridge airborne data. *Cryosphere* **2013**, *7*, 1035–1056. [CrossRef]
49. Panzer, B.; Gomez-Garcia, D.; Leuschen, C.; Paden, J.; Rodriguez-Morales, F.; Patel, A.; Markus, T.; Holt, B.; Gogineni, P. An ultra-wideband, microwave radar for measuring snow thickness on sea ice and mapping near-surface internal layers in polar firn. *J. Glaciol.* **2013**, *59*, 244–254. [CrossRef]
50. Jutila, A.; King, J.; Paden, J.; Ricker, R.; Hendricks, S.; Polashenski, C.; Helm, V.; Binder, T.; Haas, C. High-Resolution Snow Depth on Arctic Sea Ice from Low-Altitude Airborne Microwave Radar Data. *IEEE Trans. Geosci. Remote Sens.* **2021**, *60*, 1–16. [CrossRef]
51. Alexandrov, V.; Sandven, S.; Wahlin, J.; Johannessen, O.M. The relation between sea ice thickness and freeboard in the Arctic. *Cryosphere* **2010**, *4*, 373–380. [CrossRef]
52. Hendricks, S.; Ricker, R. Product User Guide & Algorithm Specification—AWI CryoSat-2 Sea Ice Thickness (version 2.3). 2020. Available online: https://www.researchgate.net/publication/346677382 (accessed on 19 December 2021).
53. Spreen, G.; Kaleschke, L.; Heygster, G. Sea ice remote sensing using AMSR-E 89-GHz channels. *J. Geophys. Res. Earth Surf.* **2008**, *113*, C02S03. [CrossRef]
54. Mallett, R.D.C.; Lawrence, I.R.; Stroeve, J.C.; Landy, J.C.; Tsamados, M. Brief communication: Conventional assumptions involving the speed of radar waves in snow introduce systematic underestimates to sea ice thickness and seasonal growth rate estimates. *Cryosphere* **2020**, *14*, 251–260. [CrossRef]
55. Tilling, R.L.; Ridout, A.; Shepherd, A. Estimating Arctic sea ice thickness and volume using CryoSat-2 radar altimeter data. *Adv. Space Res.* **2017**, *62*, 1203–1225. [CrossRef]
56. Skourup, H.; Farrell, S.L.; Hendricks, S.; Ricker, R.; Armitage, T.W.K.; Ridout, A.; Andersen, O.B.; Haas, C.; Baker, S. An Assessment of State-of-the-Art Mean Sea Surface and Geoid Models of the Arctic Ocean: Implications for Sea Ice Freeboard Retrieval. *J. Geophys. Res. Oceans* **2017**, *122*, 8593–8613. [CrossRef]
57. Ivanova, N.; Pedersen, L.T.; Tonboe, R.T.; Kern, S.; Heygster, G.; Lavergne, T.; Sørensen, A.; Saldo, R.; Dybkjær, G.; Brucker, L.; et al. Inter-comparison and evaluation of sea ice algorithms: Towards further identification of challenges and optimal approach using passive microwave observations. *Cryosphere* **2015**, *9*, 1797–1817. [CrossRef]
58. Kingma, D.P.; Ba, J. Adam: A method for stochastic optimization. In Proceedings of the International Conference Learning Representations (ICLR), San Diego, CA, USA, 5–8 May 2015.
59. Armitage, T.W.K.; Ridout, A.L. Arctic sea ice freeboard from AltiKa and comparison with CryoSat-2 and Operation IceBridge. *Geophys. Res. Lett.* **2015**, *42*, 6724–6731. [CrossRef]

60. Kwok, R. Simulated effects of a snow layer on retrieval of CryoSat-2 sea ice freeboard. *Geophys. Res. Lett.* **2014**, *41*, 5014–5020. [CrossRef]
61. Miernecki, M.; Kaleschke, L.; Maaß, N.; Hendricks, S.; Søbjærg, S.S. Effects of decimetre-scale surface roughness on L-band brightness temperature of sea ice. *Cryosphere* **2020**, *14*, 461–476. [CrossRef]
62. Derksen, C.; Burgess, D.; Duguay, C.; Howell, S.; Mudryk, L.; Smith, S.; Thackeray, C.; Kirchmeier-Young, M. Changes in snow, ice, and permafrost across Canada. In *Canada's Changing Climate Report*; Bush, E., Lemmen, D.S., Eds.; Government of Canada: Ottawa, ON, Canada, 2019; Chapter 5; pp. 194–260. Available online: https://www.nrcan.gc.ca/sites/www.nrcan.gc.ca/files/energy/Climate-change/pdf/CCCR-Chapter5-ChangesInSnowIcePermafrostAcrossCanada.pdf (accessed on 19 December 2021).